The metallic palladium-rhodium solution in interaction with oxygen: The Pd-Rh-O phase diagram and thermodynamics

C. Laurin, A. Quaini, E. Regnier, A. Laplace, T. Croze, Stéphane Gossé

The metallic palladium-rhodium solution in interaction with oxygen: The Pd-Rh-O phase diagram and thermodynamics

C. Laurin[1], A. Quaini[2], E. Regnier[1], A. Laplace[1], T. Croze[2], S. Gossé[2]*

[1] DES, ISEC, DE2D, Univ. Montpellier – Laboratoire de Développement des Matrices de Confinement – Marcoule, 30207 Bagnols-sur-Cèze Cedex, France

[2] DES, ISAS – Service de la Corrosion et du Comportement des Matériaux dans leur Environnement (SCCME), CEA, Université Paris-Saclay, F-91191, Gif-sur-Yvette, France

*Corresponding author: Stéphane Gossé (stephane.gosse@cea.fr) Tel: +33(1)69082011

Abstract

Palladium and rhodium are two metals widely used in the industry because of their high electrical and thermal conductivity and catalytic activity. In the nuclear field, both elements are also known as fission products. Due to their sensitivity towards oxygen, the thermodynamic equilibria of the Pd-Rh-O system have been assessed in this paper thanks to the Calphad method.

The linear fit of the Gibbs free energy of PdO is $\Delta_f G°_T(PdO) = -115.8 + 0.102 \cdot \mathrm{T}$ (kJ·mol^{-1}) and its calculated heat of formation is –58.994 kJ·mol^{-1}·at^{-1}. The assessed Pd(g) equilibrium pressure under 1 bar of O_2 is:

$$\log_{10} p_{Pd}(bar) = 6.560 - \frac{19046.9}{T}$$

The Pd(g) and PdO(g) equilibrium pressures at PdO decomposition are respectively:

$$\log_{10} p_{Pd}(bar) = 6.7269 - \frac{19339.0}{T}$$

$$\log_{10} p_{PdO}(bar) = 8.55 - \frac{23649.7}{T}$$

From this new Rh-O assessment, the Rh_2O_3 and RhO_2 heat of formation are –79698 kJ·mol^{-1}·at^{-1} and –80142 kJ·mol^{-1}·at^{-1}, respectively. The calculated Gibbs energy of formation of RhO_2 and Rh_2O_3 can be expressed as $\Delta G_f^{RhO_2} = -234.44 + 0.1751 \cdot \mathrm{T}$ and $\Delta G_f^{Rh_2O_3} = -389.51 + 0.2737 \cdot \mathrm{T}$ (in kJ·mol^{-1}), respectively.

Keywords

Calphad; Oxidation; Palladium; Phase diagram; Vapor pressure; Rhodium

1. Introduction

Palladium and rhodium are platinoid elements. These two metals, along with the other platinum group metals (PGMs) – iridium, osmium, platinum and ruthenium – are found all together in the earth mantle [1]. They are ones of the rarest metals [2]. Palladium and rhodium behave quite similarly in magma and usually precipitate within sulfide phases in mafic and ultramafic rocks [3,4]. Their precipitation depends on their environment and, among others, on the oxygen pressure [5]. Palladium and rhodium are highly thermally and electrically conductive [6]. Because of these interesting properties and their high catalytic activity [7,8], they are widely used in the industry.

In the nuclear field, both of these PGMs are formed by fission reactions of the nuclear fuel. During nuclear reactions, they may alloy with molybdenum, ruthenium and technetium to form metallic inclusions so-called “white phases” [9] as also observed in the natural Oklo reactor in Gabon [10]. To predict the interactions between the fuel and the cladding materials, it is important to model the thermochemistry of the nuclear fuel as a function of temperature and oxygen partial pressure. Especially in case of a severe nuclear accident with air ingress or during the reprocessing steps of the spent fuel, palladium and rhodium may behave as semi-volatile fission products. Their volatilization into Pd(g), PdO(g), Rh(g), RhO(g) and RhO_2(g) strongly depends on the oxygen partial pressure [11]. These gaseous species phase are responsible for a part of radionuclides emission during a severe nuclear accident and the conditions of its formation must be known to prevent environmental release [12-14].

In many countries, the spent nuclear fuel is reprocessed and these PGMs are vitrified within a high-level waste glass with other fission products. Nevertheless, these two transition elements are poorly soluble in the reference R7/T7 borosilicate matrixes [15-18]. Unlike most fission products, palladium and rhodium may form oxide or metallic precipitates [15,18,19] in the waste glasses. They strongly partitionate like in silicate melts and igneous rocks [20]. Palladium and rhodium also show partitioning between siderophile and chalcophile melts; they both exhibit a strong affinity towards chalcogen elements (S, Se, Te) [21]. In nuclear waste glasses, palladium exhibits a slightly more chalcophile behavior than rhodium [22]. Palladium forms intermetallics with tellurium whereas rhodium is partitioned between these phases and the rutile structure compound $(Ru,Rh)O_2$ [12,18,19,23].

Therefore, the thermodynamic properties of the Pd-Rh-O system and the related phase diagram must be assessed in order to meet both the industrial and geological issues. This study complements the Pd-Rh-Ru and Ru-Rh-O thermodynamic models [12,24] already developed for these PGMs.

2. Thermodynamic modeling

The thermodynamic modeling was performed with the Calphad method [25]. This method enables the determination of the equilibrium states of a chemical system by the minimization of the Gibbs energy functions of possibly formed phases. The Gibbs energy of the phases is referred to the enthalpy of the pure elements at 298.15 K and 1 bar, in their stable physical state, $°H_i^{SER}(298.15\ K)$. These elements are qualified as "SER" for "Stable Element Reference". The expression of Gibbs energy functions depends on the phase type described.

2.1. Pure elements Pd, Rh and O

The expression of the Gibbs energy of the pure element *i* at temperature *T* in its state φ, $°G_i^{\varphi}(T)$, is expressed according equation 1:

$$°G_i^{\varphi}(T) - °H_i^{SER}(298.15\ K) = a + bT + clnT + \sum_n d_n T^n \quad (1)$$

With *n* an integer usually 2, 3 or -1 and *a*, *b*, *c* and d_n adjustable coefficients.

2.2. Oxide phases

All the oxide phases i.e. PdO, RhO_2 and Rh_2O_3 are modeled as stoichiometric compounds. The Gibbs energy of the oxide *Ox*, formed of element *A* and *B*, at temperature *T*, $°G^{Ox}(T)$, is written in equation 2:

$$°G^{Ox}(T) - \sum_{A,B} x_i °H_i^{SER}\ (298.15\ K) = a + bT + clnT + \sum_n d_n T^n \quad (2)$$

With x_A and x_B the atomic fraction of components A and B in the stoichiometric oxide, *n* an integer and *a*, *b*, *c* and d_n adjustable coefficients.

2.3. FCC solid solution and metallic liquid phase

A solid solution φ of two elements A and B is described by a two sublattice model [26], as for metallic liquid defined according to the two-sublattice ionic model [27]. The expression of the Gibbs energy of these phases are the sum of the reference Gibbs energy G^{φ}_{ref}, the Gibbs energy of the ideal mixture G^{φ}_{id}, and the excess Gibbs energy G^{φ}_{ex} (equation 3):

$$G^{\varphi}(T) - \sum_{A,B} x_i °H_i^{SER}\ (298.15\ K) = G^{\varphi}_{ref} + G^{\varphi}_{id} + G^{\varphi}_{ex} \quad (3)$$

The expression of each contribution to the Gibbs energy function is developed in equation 4, 5 and 6:

$$G^{\varphi}_{ref} = \sum_{A,B} x_i \left(°G_i^{\varphi}(T) - °H_i^{SER}(298.15\ K)\right) \quad (4)$$

$$G^{\varphi}_{id} = RT \sum_{A,B} x_i lnx_i \quad (5)$$

With *R* the ideal gas constant.

$$G_{ex}^{\varphi} = x_A x_B \sum_n {}^n L_{A,B}(x_A - x_B)^n \quad (6)$$

With n = 0, 1, 2 and ${}^n L_{A,B}$ Redlich & Kister polynomial formula for the mixture between *A* and *B* [28], described by the equation 7:

$${}^n L_{A,B} = a + bT \quad (7)$$

2.4. Gas phase

The gas phase is considered as an ideal mixture of gaseous species (O, O_2, O_3, Rh, RhO, RhO_2, Pd, PdO). The Gibbs energy of the gas phase is given in equation 8:

$$G^{\varphi} = \sum_i x_i \, {}^\circ G_i + RT \sum_i x_i \, ln x_i + RT ln \frac{p}{p_0} \quad (8)$$

With p the pressure of the gas phase and p_0 the reference pressure.

3. Thermodynamics and phase diagrams of binary systems

3.1. The Pd-Rh system

The Pd-Rh system was previously reviewed by Gossé et al. [24]. Nevertheless, this assessment did not consider all the EMF (electromotive force) measurements from Jacob et al. [29]. In this new version, some minor corrections were applied to better assess the full range of their EMF results in the binary alloys. The results from Table 1 and Eq. 2 in [29] were used to reassess the interaction parameters in the fcc solid solution; the calculated Rh activity are compared with those obtained from EMF results (Figure *1a*). Using this new modeling, the Pd and Rh chemical activities were recalculated and compared with the activities from torsion-effusion vapor pressures measurements at 1575 K from Myles [30], the EMF data at 1273 K from Jacob et al. [29] and the former assessment by Gossé et al. [24] (Figure *1b*).

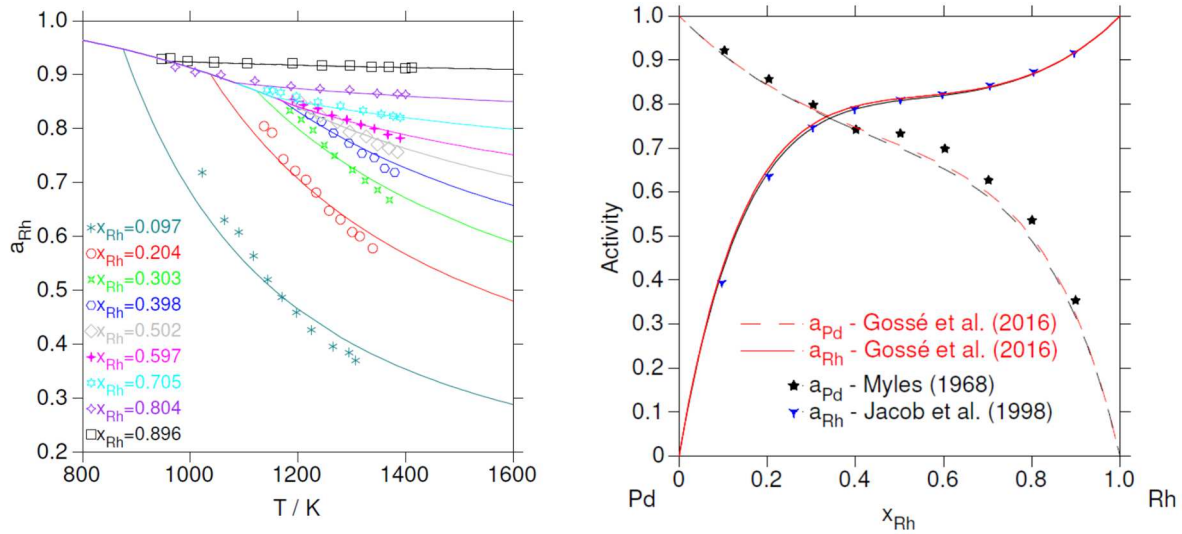

a) *b)*

Figure 1: a) Calculated Rh chemical activity for x_{Rh} = 0.097, 0.204, 0.303, 0.398, 0.502, 0.597, 0.705, 0.804, 0.896, comparison with Jacob et al. [29], b) Calculated Pd chemical activity at 1575 K and Rh chemical activity at 1273 K, comparison with literature data [24,29,30]

Liquid parameters were reassessed because of the new thermodynamic description of the fcc solution. No changes were made to the metastable hcp solution in Pd-Rh. The new Pd-Rh parameters are listed in Appendix 1. Using these new optimized values, the Pd-Rh phase diagram is calculated (Figure 2). No significant feature appears between this diagram and the previous assessment by Gossé et al. [24].

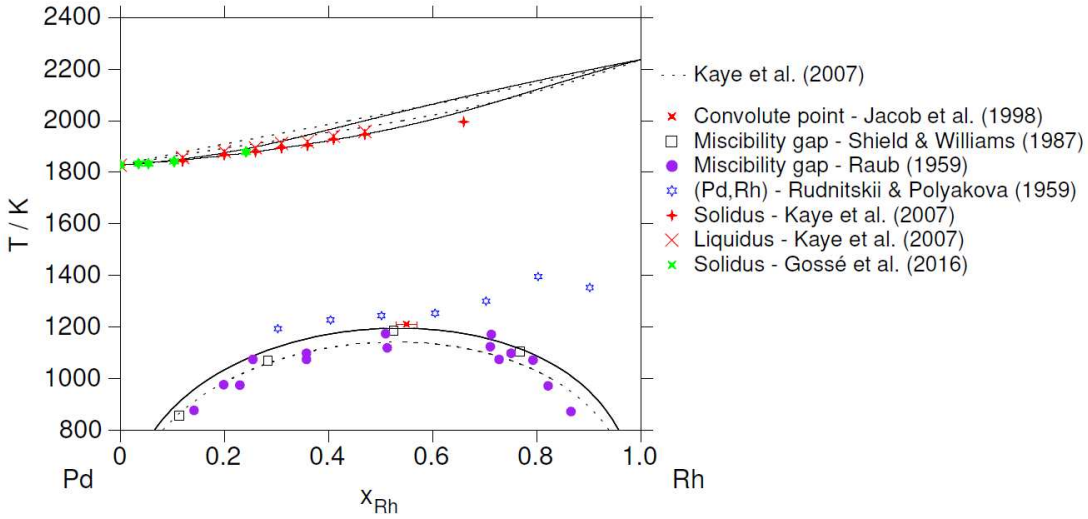

Figure 2: Calculated Pd-Rh phase diagram, comparison with experimental literature data [29,31-34] and previous thermodynamic assessments [24,34]

3.2. The Rh-O system

The Rh-O system was previously reviewed by Gossé et al. [12]. The stable solid oxides in this system are RhO_2 and Rh_2O_3. RhO_2 has a rutile structure [35] whereas Rh_2O_3 has a corundum structure [36]. Above approximately 1200 K, Rh_2O_3 exhibits an allotropic transition towards an orthorhombic structure [37].

With increasing temperature and decreasing oxygen pressure, RhO_2 decomposes into Rh_2O_3, then Rh_2O_3 decomposes into metallic fcc-Rh. Several authors experimentally assessed the decomposition of Rh_2O_3 into fcc-Rh [35,38-43]. Nell & O'Neill [42] and Jacob et al. [29,43] performed EMF measurements to determine the enthalpy of formation and/or the Gibbs free energy of Rh_2O_3. Jacob & Prusty [44] implemented the same experimental method for RhO_2. Both these accurate results are used for this updated assessment. Figure 3*a* compares these literature data with the calculated Rh_2O_3 and RhO_2 heat of formation. The calculated Rh_2O_3 heat of formation is - 79.698 kJ·mol^{-1}·at^{-1} in very good agreement with Nell & O'Neill [42], Jacob & Sriram [45] and Bayer & Wiedemann [46]. The calculated RhO_2 heat of formation is - 80.142 kJ·mol^{-1}·at^{-1}; this result is very close to - 81.647 ± 0.060 kJ·mol^{-1}·at^{-1} after Jacob & Prusty [44] (Figure 3*a*).

In the present modeling, further attention was paid to the formation enthalpies of Rh_2O_3 and RhO_2, but some inconsistencies remained due to the scattered formation enthalpy of Rh_2O_3. Part of the lack of consistency comes from many third law analyses based on only estimated Cp data. The Gibbs energy of Rh_2O_3 is also scattered; the calculated functions were compared to Jacob et al. [43], Mallika et al. [39], Nell & O'Neill [42] and Kleykamp [38]; the assessed Gibbs free energy of Rh_2O_3 is very close to Mallika et al. [39] results (Figure 3*b*). In the temperature range 400-1400 K, the new linear fits of the Gibbs energy of formation of Rh_2O_3 and RhO_2 (kJ·mol^{-1}) vary as follow (Equations 9 & 10):

$$\Delta G_f^{Rh_2O_3} = -389.5 + 0.2737 \times \mathrm{T}\ (\mathrm{kJ{\cdot}mol^{-1}}). \quad (9)$$

$$\Delta G_f^{RhO_2} = -234.44 + 0.1751 \cdot \mathrm{T}\ (\mathrm{kJ{\cdot}mol^{-1}}) \quad (10)$$

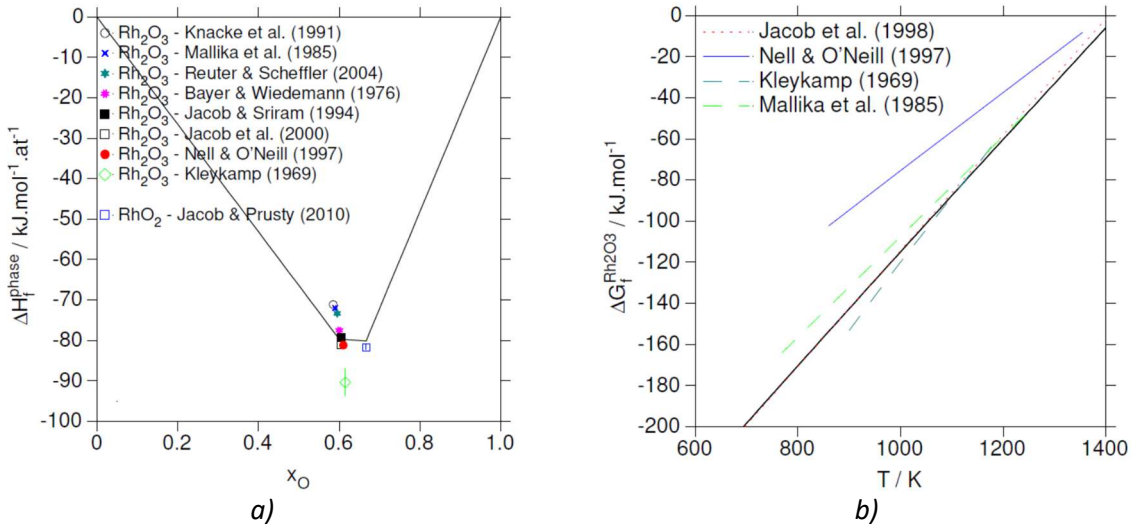

Figure 3: a) Calculated Rh_2O_3 and RhO_2 heat of formation in kJ·mol^{-1}·at^{-1}, comparison with literature data [38,39,42-45,47-49], b) Calculated Rh_2O_3 Gibbs free energy in kJ·mol^{-1}, comparison with literature data [29,38,39,42]

Still this new assessment is consistent with the oxygen pressure data [35,38-44,47]; these oxygen equilibrium pressures were recalculated for Rh_2O_3 (Figure 4*a*) and for RhO_2 (Figure 4*b*).

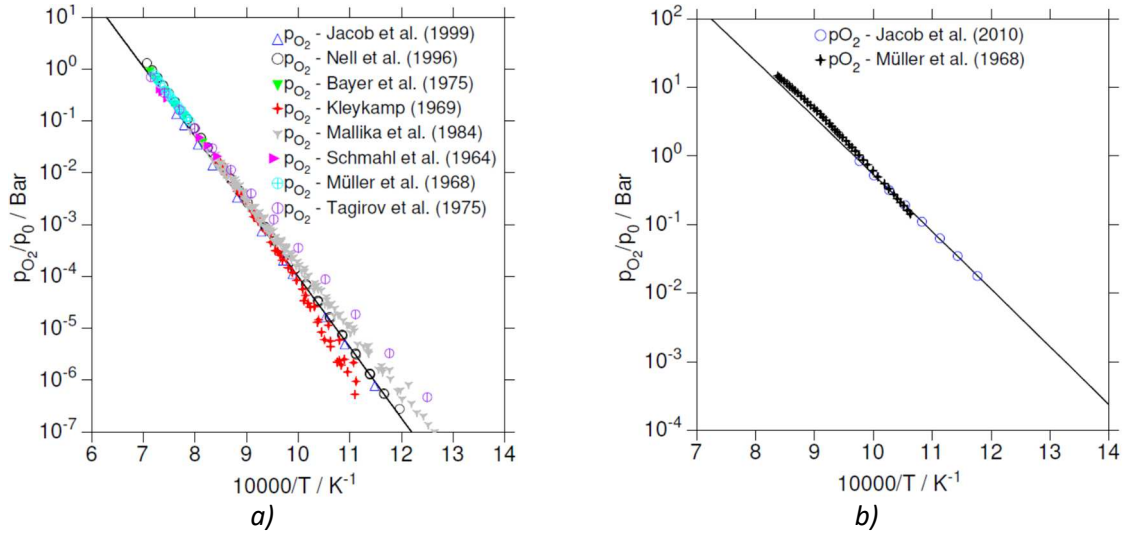

Figure 4: a) Calculated equilibrium oxygen pressure (referenced to p_0 = 1 bar) at Rh_2O_3 decomposition as a function of 10000/T (in K^{-1}), comparison with literature data [35,38-43,47], b) Calculated equilibrium oxygen pressure (referenced to p_0 = 1 bar) at RhO_2 decomposition as a function of 1000/T (in K^{-1}), comparison with literature data [35,44]

According to this new modeling of the Rh-O system, the calculated decomposition temperatures of rhodium oxides at p = 1 bar are 1399 K and 1035 K for Rh_2O_3 and RhO_2, respectively.

3.3. The Pd-O system

The Pd-O system was not assessed yet and no binary Pd-O phase diagram has been drawn ever. However, some thermodynamic properties of the Pd-O binary system were determined in literature. Several authors [50; 51; 52; 53; 54; 55] studied PdO heat capacity and enthalpic increment. Among them, the values after Kubaschewski et al. [54] and Rao [55] are inconsistent with the other ones. From these results, the heat capacity and the enthalpic increment of PdO is modeled; the thermodynamic data from Kubaschewski et al. [54] and Rao [55] were not used.

Heat capacity and enthalpic increment of PdO

The heat capacity (C_p) of PdO was determined by DSC measurements by Nell & O'Neill [52] and Jacob et al. [53] from 370 K to 1050 K. Khodakovskii et al. [50] used an adiabatic vacuum calorimeter within a temperature range of 268.33-328.86 K; the higher temperature values (*i.e.* from 400 to 1300 K) were not measured but calculated.

All sets of data are coherent with each other, except for a slight deviation after Jacob et al. [53] at high temperature. Smirnova et al. [51] are the only ones who measured the C_p for temperatures lower than 350 K. Their low temperature results overlap properly with C_p at higher temperature. Nell & O'Neill [52] proposed a heat capacity relation of PdO in the 370 K-1065 K range expressed by the equation 11:

$$C_P = 71.08 - 531.6T^{-0.5} \ (J \cdot mol^{-1} \cdot K^{-1}) \quad (11)$$

The comparison between the retained literature data and the assessed C_p of PdO is displayed on Figure 5*a*. The modeling fits well with the data from Smirnova et al. [51] above 200 K and Nell & O'Neill [52] at higher temperature; it is also fairly consistent with Khodakovskii et al. [50] and Jacob et al. [53].

From their C_p measurements, Khodakovskii et al. [50] deduced the enthalpic increment of PdO in the temperature range of 298.15-1300 K. As for C_p of PdO, data after Rao [55] were discarded. The enthalpic increment of PdO is therefore fitted after Khodakovskii et al. [50] in Figure 5*b*.

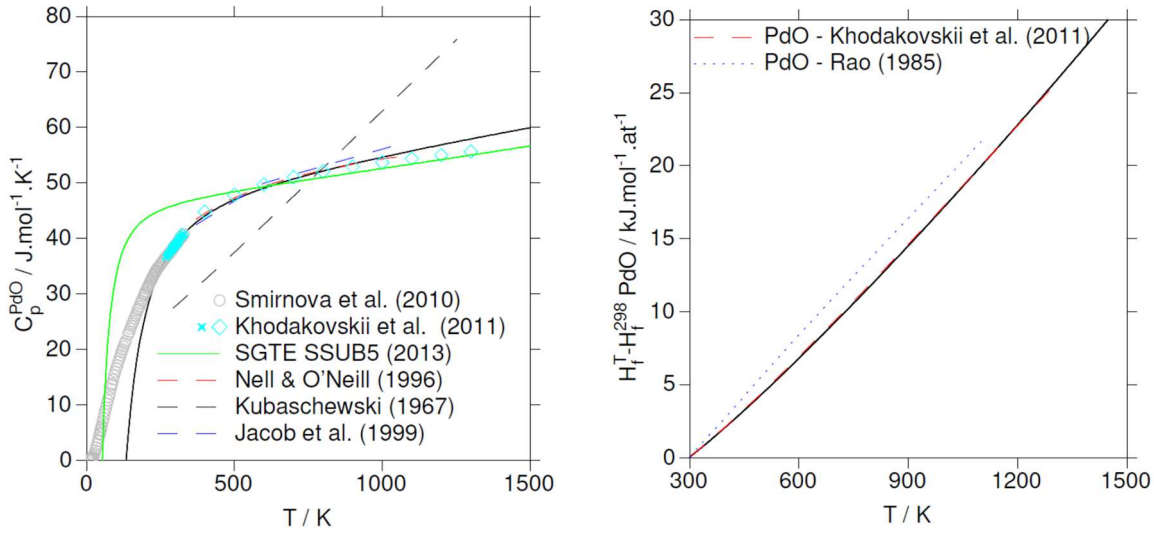

Figure 5: a) Calculated PdO heat capacity in J·mol^{-1}·K^{-1} (black full line), comparison with [50-54,56], b) Calculated PdO enthalpic increment in kJ·mol^{-1}·at^{-1}, comparison with literature data [50,55]

Formation enthalpy and Gibbs energy

Numerous standard enthalpies of formation and Gibbs energies of PdO are available in literature. Nell & O'Neill [52] and Mallika et al. [57] provided an almost complete review of these thermodynamic values. They are summarized in Table 1.

Authors	Method	Standard formation enthalpy $\Delta_f H^\circ_{298}$ (kJ·mol^{-1})	Gibbs free energy (J·mol^{-1})	Temperature (K)
Mallika et al. [57]	EMF	- 116.25 ± 0.41	- 112790 + 0.0998·T ± 274	699-1060
Nell & O'Neil [52]	EMF	- 117.42 ± 0.3	- 119421 + 158.06·T - 7.6·T·lnT ± 40 T > 800 K and ± 200 T < 800K	730-1200
Kleykamp [58]	EMF	- 118.1 ± 2.1	- 114970 + 100.1·T ± 1172	1000-1140
Pawlas-Foryst & Zabdyr [59]	EMF	- 115.45 ± 1.1	- (111000±1.1) + (88 ± 1.1) T	843-1100
Jacob et al. [29]	EMF		- 110040 + 95.81·T ± 120	950-1350
Jacob et al. [53]	EMF	- 115.51 ± 0.13	- 111920 + 97.87·T ±120	
Fouletier et al. [60]	EMF		- 111250 + 97.2·T	725-1000
Levitskii et al. [61]	EMF		- 109500 + 96·T	800-1040
De Bruin & Badwal [62]	Impedance	- 121.01 ± 0.8	- (113900 ± 750) + (99.9 ± 1.5) T	935-1140
Bayer & Wiedemann [46]	Thermal dissociation	- 114.6 (dissociation)	- 114520 + 100.4·T	962-1150
Tagirov et al. [41]	Thermal dissociation		- 126930 + 143·T	720-800
Bell et al. [63]	Transpiration, static p(O_2)	- 112.2	- 107950 + 94.1·T	950-1150
Warner [64]	Static p(O_2)	- 118.595 ± 1.67	- 11300 + 60·T·logT - 26·T² - 41840·T^{-1} - 50·T	910-1145
Schmahl & Minzl [40]	p(O_2)		- 106740 + 93·T	1025-1115
Khodakovskii et al. [50]	DSC	- 115.8±4.5		

Table 1: Summary of the experimental standard enthalpy of formation and Gibbs free energy of PdO from literature

Nell & O'Neill [52] measured the Pt, Pd + PdO | Calcia-Stabilized Zirconia electrolyte | air, Pt cell EMF between 730 K and 1200 K to determine the Gibbs free energy of formation of PdO. Mallika [57] used a similar method with an Yttria-Stabilized Zirconia electrolyte.

Jacob et al. [53], Pawlas-Foryst & Zabdyr [59] and Fouletier et al. [60] also used a galvanic cell in their study for narrower temperature range. Kleykamp [58] used Fe+FeO reference electrode , while Jacob et al. [29] used Rh + Rh_2O_3. Bell et al. [63] and Warner [64] applied the method of static oxygen pressure and deduced the relation between p(O_2) and temperature. The relation obtained by Nell & O'Neill [52] is defined in equation 12:

$$\begin{aligned}\log f_{O_2} = {} & 16.510\text{-}12473.4\cdot T^{-1}\text{-}1.826\cdot \log T \\ & + p\left[0.0627\cdot T^{-1}\text{-}5.22\cdot 10^{-7}\left(1\text{-}298\cdot T^{-1}\right)+10^{-8}\cdot p\cdot T^{-1}\right]\end{aligned} \quad (12)$$

With f_{O_2} the oxygen fugacity referenced to a standard state of 1 bar, *T* the temperature in K and *p* the total pressure in bar. All these authors gave the Gibbs energy of formation of PdO ($\Delta_f G^\circ$). Results are given for the reaction Pd(s) + ½ O_2(g) → PdO(s)

All the data are consistent, and they are displayed on Figure 6*a*. In the temperature range 400-1200 K, the expression of the calculated Gibbs energy of formation of PdO from the present Calphad assessment is (Equation 13):

$$\Delta_f G°_T(PdO) = -115.8 + 0.102 \cdot T \ (kJ \cdot mol^{-1}) \quad (13)$$

The standard enthalpy of formation of PdO ($\Delta_f H°_{298K}$) in the PtS structure is calculated in some of these papers [50; 52; 53; 57; 58; 59; 62; 63; 64]. The higher value is - 112.2 kJ·mol^{-1} and the lower one is - 121.01 kJ·mol^{-1}. The value after Khodakovskii et al. [50] is discarded due to the relatively high uncertainty of $\Delta_f H°_{298}$. Moreover, $\Delta_f H°_{298K}$ results after De Bruin & Badwal [62], Bayer & Wiedemann [46] and Bell et al. [63] display slight discrepancies and are not retained for database optimization. The thermodynamic study of Nell & O'Neill [52] is complete and their results are acquired by direct measurements and applicable on a wide range of temperature. For these reasons, these data are thoroughly used thereafter. Enthalpy of formation of PdO is compared with literature data (in kJ·mol^{-1}): Mallika et al. [57] - 116.248 ± 0.41, Kleykamp [58] - 117.989 ± 2.094 and Nell & O'Neill [52] - 117.420 ± 1.000 (estimated error by the authors). All these data are very coherent, and the assessed result displays a very good consistency with them: - 115.944 kJ·mol^{-1} (Figure 6*b*).

Persson run DFT simulations of the PdO halite structure ($Fm\bar{3}m$, NaCl prototype) using GGA approximation with 520 eV cutoff energy [65]. The calculated PdO enthalpy of formation was - 0.348 eV·at^{-1} (i.e. -33.577 kJ·mol^{-1}·at^{-1}). The difference between this value and the assessed PdO enthalpy of formation within the PtS structure was used to establish the Gibb energy of the $(Pd)_1(O)_1$ end-member in the fcc structure.

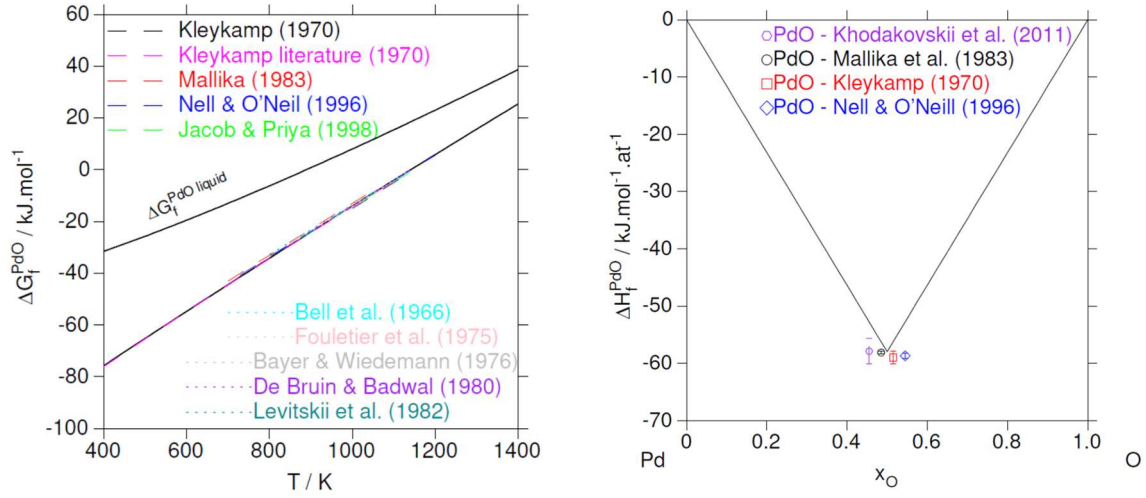

a) *b)*

Figure 6: a) Calculated PdO Gibbs free energy (solid & liquid), comparison with literature data [29,46,52,57,58,60-63] , b) Calculated PdO heat of formation in kJ·mol^{-1}·at^{-1} (slightly shifted for a better lecture), comparison with literature data [52,57,58]

Norman et al. [13] and Olivei [66] are the only authors reviewed who calculates thermodynamic parameters of $PdO_{(g)}$. They studied the reaction $Pd_{(s)} + ½\ O_2 \rightarrow PdO_{(g)}$ thanks to a Knudsen cell and a Langmuir cell, respectively. Norman et al. [13] gave $\Delta H°_{298K}\ (PdO_{(g)})$ = 349.2 ± 12.6 kJ·mol^{-1} and $\Delta S°_{298K}\ (PdO_{(g)})$ = 78.7 ± 10.5 J·mol^{-1}·K^{-1}. Olivei [66] calculated $\Delta_f G°_T$ between 900 and 1700 K, from 273 kJ·mol^{-1} at 900 K to 214 kJ·mol^{-1} at 1700 K.

Using third-law of thermodynamics, some authors also calculated the standard entropy of PdO, $S°_{298K}$. These results are shown in Table 2. The standard entropy given by De Bruin & Badwal [62] and Nell & O'Neill [52] is lower than most of the calculations. According to [46; 50; 59; 63], the

standard entropy of formation or dissociation of PdO ΔS°_{298K} is around 100 J·mol^{-1}·K^{-1}. The entropy calculated by Jacob et al. [53], which has been determined thanks to EMF measurements (direct method), is the target for our optimization.

Authors	Standard entropy J·mol^{-1}·K^{-1}
Nell & O'Neill [52]	33.74 ± 0.3
Kleykamp [58]	36.8 ±2.1
Warner [64]	36.0 ± 1.3
De Bruin & Badwal [62]	33.5 ±1.5
Khodakovskii et al. [50]	36.5 ±4.0
Pawlas-Foryst & Zabdyr [59]	39.83 ± 1.1
Jacob et al. [53]	37.25 ± 0.4

Table 2: Summary of the standard entropies of PdO calculated in the literature

PdO decomposition temperature

PdO is the only existing binary palladium oxide; several authors studied the structural properties of this so-called Cooperite mineral [67].

PdO has a *P4$_2$/mmc* tetragonal structure [46; 68] and the lattice parameters of this PtS prototype are a = 0.3043 ± 0.0004 nm, c = 0.5337 ± 0.0004 nm [68]. Many studies determined the decomposition temperature of this oxide by direct experiments or by indirect methods [29; 40; 46; 57; 63; 69]. The predicted PdO decomposition temperature at $p(O_2)$ = 1 bar is between 1124 K and 1150 K. To avoid any propagation of uncertainties, direct measurements of the decomposition temperature is preferred to fitting of Gibbs free energy functions. Therefore, results after Mallika et al. [57] and Jacob et al. are not considered [29; 57]. The 1150 K decomposition temperature determined by Bayer and Wiedemann [46] is ruled out since they use only one heating rate for DTA. Zhang et al. [69] measured a decomposition temperature of PdO of 1124 K thanks to DTA too. This value was dismissed because of the lack of tracking of oxygen pressure and the lack of linearity of the curve $p(O_2)=f(1/T)$. The most accurate value seems to be acquired by Bell [63] with a reaction cell. The decomposition temperature of PdO is thus appraised to be around 1143 K. This value is moreover in good agreement with temperatures given by Jacob et al. [29] and Mallika et al. [57]. Experimental results along with calculated Pd-O phase diagram are display on Figure 7*a*.

Oxygen solubility

The oxygen solubility in metallic Pd was studied by Gegner et al. [70], Wang & Flanagan [71], Park & Altstetter [72] and Raub & Plate [73]. Gegner et al. [70] used an oxygen desorption method in an ultra-high vacuum vessel. They quantified the oxygen solubility thanks to pressure measurements. Wang & Flanagan [71] determined the solubility by titrating dissolved O with gaseous H. Park & Altstetter [72] used an electrochemical cell and Raub & Plate [32], weight difference measurements. Because Gegner et al. [70] measured oxygen solubility at low oxygen partial pressure (0.027 bar < $p(O_2)$ < 0.4 bar), the value of 0.056 at% given at 1123 K and 1 bar is only an extrapolation. However, this value is in good agreement with Wang & Flanagan's [71] results: 0.065 ± 0.001 at% at 1073 K, 0.052 at% at 1123 K, 0.042 at% at 1173 K and 0.032 at% at 1223 K. Jehn & Grallath's results mentioned in [71] gives a solubility slightly higher but in the same order of magnitude [74]. The solubility given by Raub & Plate [32; 72] and by Park & Altstetter [32; 72] are excluded because they are significantly higher and lower than the previous ones, respectively. The optimization is thus mainly performed on the results after Wang & Flanagan [71] and Jehn & Grallath [74]. Figure 7*b* shows the solubility of oxygen in fcc-Pd fitted on experimental data.

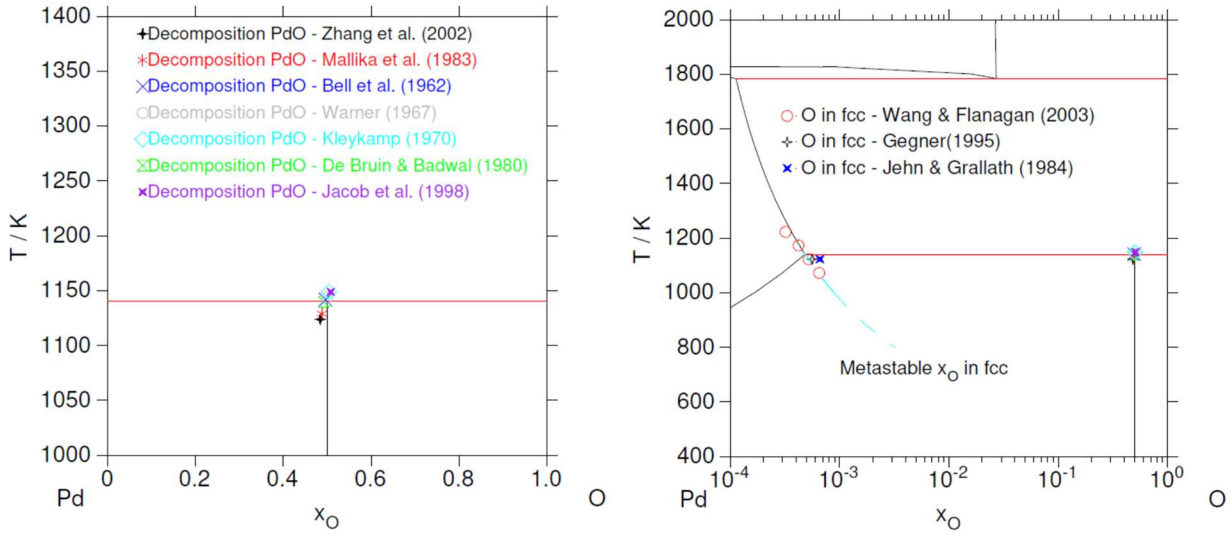

Figure 7: a) Calculated Pd-O phase diagram, comparison with experimental PdO decomposition temperature [29,57,58,62-64,69] b) Zoom on the calculated O solubility in the Pd(O) fcc solid solution, comparison with experimental results from [70,71,74]

Equilibrium vapor pressure

Under an oxidative atmosphere, PdO can be vaporized. Norman et al. [13] and Matsui & Naito [75] studied $Pd_{(g)}$ and $PdO_{(g)}$ volatilization from pure $Pd_{(s)}$ and from Mo-Ru-Pd alloys using Knudsen Effusion Mass Spectrometry (KEMS) and thermodynamic calculations, respectively. Matsui & Naito [75] expounded that, unlike many metals, the vapor pressure of the gaseous metal Pd(g), over solid oxide PdO(s), is higher than that of PdO(g). At 1 bar of O_2 and 1000 K, Norman et al. [13] stated that the palladium vapor pressure in the temperature range of 1485-1710 K is governed by equation (14):

$$\log_{10} p_{Pd}(atm) = 6.120 - \frac{19370}{T} \quad (14)$$

Previously, Alcock & Hooper [14] gave a similar equation in equation (15) but established only from two measurements (1673 K and 1773 K):

$$\log_{10} p_{Pd}(atm) = 8.62 - \frac{23450}{T} \quad (15)$$

Both equations are in good agreement. Nevertheless, the equation after Norman et al. [13] was considered to be more accurate. Even if they were not used for the assessment, these results were compared to the calculated vapor pressure in Figure 8*a*. The assessed Pd(g) pressure under 1 bar of O_2 is given in equation (16):

$$\log_{10} p_{Pd}(atm) = 6.560 - \frac{19046.9}{T} \quad (16)$$

The equilibrium vapor pressures of Pd(g) and PdO(g) during PdO decomposition is also represented between 1250 and 2500 K on Figure 8*b*. The assessed vapor pressures of Pd(g) and PdO(g) at PdO decomposition are listed in equations (17) and (18), respectively:

$$\log_{10} p_{Pd}(bar) = 6.727 - \frac{19339.0}{T} \quad (17)$$

$$\log_{10} p_{PdO}(bar) = 8.550 - \frac{23649.7}{T} \quad (18)$$

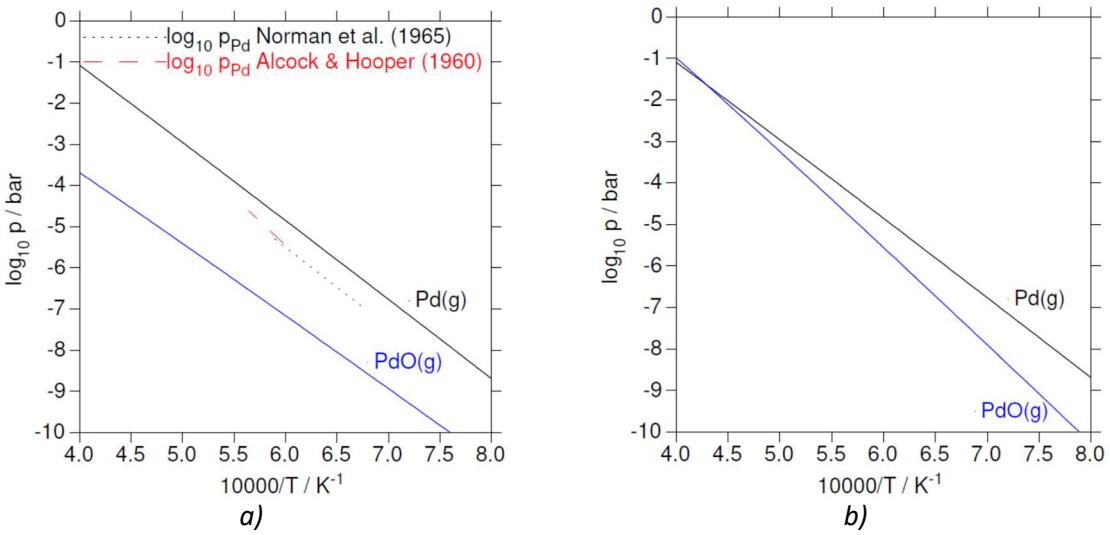

Figure 8: a) Calculated equilibrium vapor pressure of Pd(g) and PdO(g) under 1 bar of O_2, comparison with literature data [13,14], b) Calculated equilibrium oxygen pressure at PdO decomposition; in both cases, Pd(g) is more volatile than PdO(g) in a large temperature range.

4. Thermodynamics and phase diagrams of Pd-Rh-O ternary system

4.1. Review of the Pd-Rh-O system

Only Jacob et al. [29] studied this ternary phase diagram using a working electrode $Pd_{1-x}Rh_x$ + Rh_2O_3 to perform EMF measurements and to acquire reliable thermodynamic parameters of the Pd-Rh-O system. To check for the formation of ternary oxides in pseudobinary system PdO-Rh_2O_3, Jacob et al. performed some high temperature heat treatments at 1123 K for 6 days using PdO + Rh_2O_3 pellets sealed under evacuated quartz ampoules. The XRD analyses of quenched samples exhibited no evidence of solid solution or ternary phase.

Jacob states that oxygen solubility in Pd-Rh alloy is negligible. Only the fcc solid solutions $Pd_{1-x}Rh_x$ & $Rh_{1-x}Pd_x$, the oxides PdO & Rh_2O_3 and O_2 gas are considered. As already mentioned in the Pd-Rh section, Pd and Rh exist both in fcc structure and alloy easily with, yet, a miscibility gap (critical point at 1210 ± 5 K and x_{Rh} = 0.55 ± 0.02). However, in presence of oxygen, Rh_2O_3 formation is favored (at x_{Rh}=x_{Pd}=0.5 in air, Rh_2O_3 disappears at T > 1300 K). From their results, they proposed two isothermal sections of the ternary diagram at 1000 K and 1250 K (Figures 13 & 14 in [29]).

4.2. Thermodynamic modeling of the Pd-Rh-O system

The ternary Pd-Rh-O system was modeled from the present Pd-O modeling and from this updated version of the Pd-Rh assessment slightly modified from Gossé et al. [24]. The Rh-O modeling was also slightly upgraded from Gossé et al. [12] to better consider the formation enthalpy of RhO_2 and Rh_2O_3. Furthermore, some estimated interaction parameters were introduced in the two sublattice ionic liquid model between metallic and oxide binary compositions: Pd $(Pd^{+2})_2(Va^{-2})_2$ & PdO $(Pd^{+2})_2(O^{-2})_2$ and Rh $(Rh^{+4})_4(Va^{-4})_4$ & Rh_2O_3 $(Rh^{+3})_2(O^{-2})_3$. These variables avoid an ideal behavior between both Pd-PdO and Rh-Rh_2O_3 metallic and oxide (metastable) liquids, respectively.

The calculated ternary diagrams at 1000 K and 1250 K are displayed in Figure 9*a* and Figure 9*b*, respectively. These isothermal sections are compared with the ternaries after Jacob et al. [29]. Both sets of diagrams at 1000 K and 1250 K are in very good agreements despite the oversight by Jacob et al. to represent RhO_2 still stable at 1000 K. Furthermore, the oxygen pressures calculated at 1000 K in both three-phase equilibria: fcc-Pd + PdO +Rh_2O_3 and fcc_1-(Pd,Rh) + fcc_2-(Pd,Rh) +Rh_2O_3 show excellent agreements with the experimental results by Jacob et al. [29] (Figure 9*a*). The RhO_2

decomposition temperature – formerly estimated around 1023 K [35; 47] and calculated at 1033 K [12] – is now predicted at 1031 K.

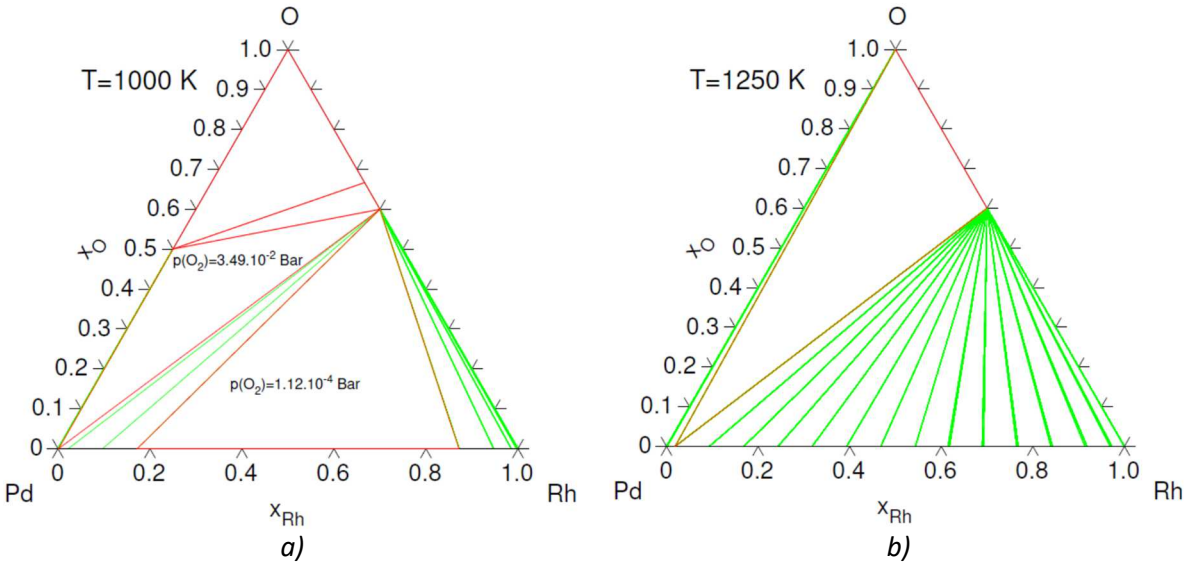

Figure 9: Calculated Pd-Rh-O isothermal sections at a) 1000 K, b) 1250 K. The calculated pressures in a) are very similar to the experimental ones in the phase diagrams by Jacob et al. [29] at 1000 K

3. Application and discussion

This modeling of the ternary system Pd-Rh-O allows to better predict the high temperature thermochemistry of these PGMs under oxidizing environments. To highlight the application of such thermodynamic assessment, Figure 10*a* exhibits the equilibrium phases as a function of temperature and oxygen pressure for a $Pd_{60}Rh_{40}$ alloy corresponding to a Pd/Rh = 1.5 molar ratio. Because of the miscibility gap between Rh and Pd depicted in Figure 2, Rh_2O_3 may be in equilibrium with two fcc solid solutions (*i.e.* $fcc_1 + fcc_2$) at low temperature and low oxygen pressure; one composition set is rich in Pd and the other one is rich in Rh with nearly reciprocal compositions due to the very symmetric fcc miscibility gap.

A higher oxygen pressure induces the oxidation of palladium, and Rh_2O_3 and PdO coexist. These calculated phases are consistent with the ternary phase diagrams at 1000 K, calculated and displayed by Jacob (Figure 9*a*). At temperature above 1193 K, the fcc miscibility gap no longer exists, and Pd and Rh are mixed within a single solid solution. Rhodium and palladium are partly soluble in each other fcc phase. For instance, at 1000 K, Pd and Rh are miscible for a Pd/Rh molar ratio lower than 0.15 or higher than 4.88 (Figure 2).

As shown on Figure 9*a*, RhO_2 is in equilibrium with Rh_2O_3 and PdO at 1000 K. At higher oxygen content, it is in equilibrium with PdO and O_2(g). This occurrence of RhO_2 at high oxygen content is exhibited in Figure 10*a*.

To highlight the low sensitivity of these binary alloys towards redox behavior, the oxygen pressure of several alloys are calculated as a function of the inverse temperature: $Pd_{80}Rh_{20}$, $Pd_{60}Rh_{40}$, $Pd_{40}Rh_{60}$ and $Pd_{20}Rh_{80}$. These compositions are compared to pure Pd in equilibrium with its oxide PdO in Figure 10*b*.

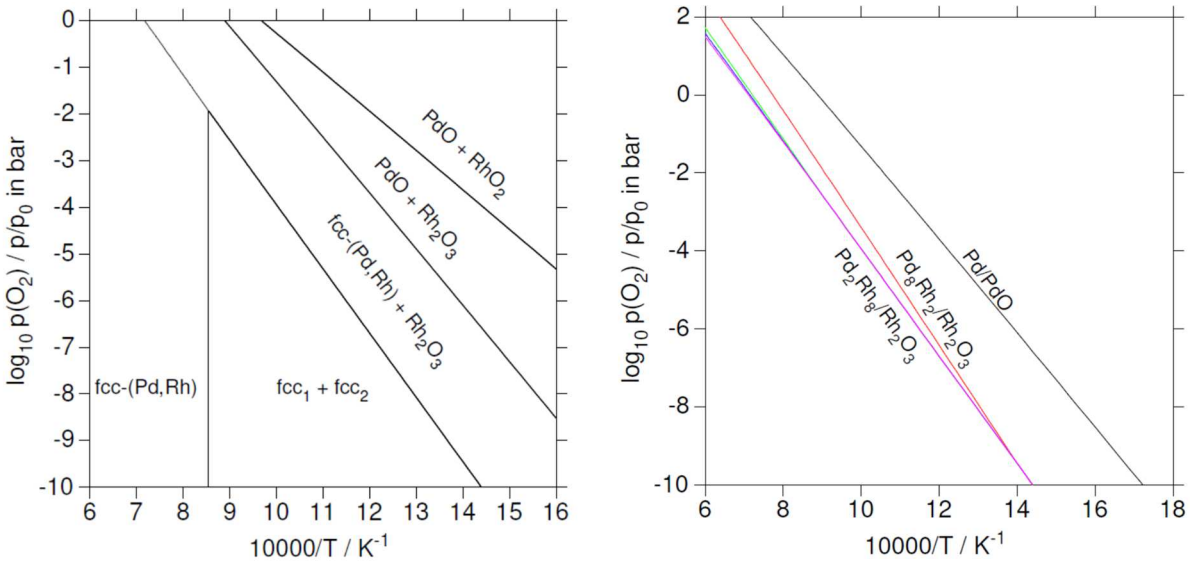

Figure 10: a) Calculated redox equilibria as a function of oxygen pressure and 10000/T (in K^{-1}) for a $Pd_{60}Rh_{40}$ alloy (in mol.%), b) Calculated redox equilibria for pure Pd and for Pd-Rh alloys: $Pd_{80}Rh_{20}$ (red) $Pd_{60}Rh_{40}$ (green) $Pd_{40}Rh_{60}$ (blue) $Pd_{20}Rh_{80}$ (pink) as a function of oxygen pressure and 10000/T (in K^{-1}) for a Pd/Rh molar ratio of 9 (90 mol.% of Pd)

4. Conclusion

The aim of this work is to predict the thermodynamics of Pd-Rh alloys under oxidative conditions in the framework of catalysis (oxidation), geochemistry and nuclear fuel applications (source term release during severe accident, fuel chemistry). This assessment is based on a thorough analysis of the literature about the Pd-Rh, Rh-O and Pd-O binaries and on the Pd-Rh-O ternary system. The resulting Calphad modeling is consistent with numerous available thermodynamic and phase diagram data.

The binary system Pd-Rh was previously assessed [24; 76]. However, the present model is largely improved by considering EMF experimental data after Jacob et al. [29]. This slight change of the interaction parameters of the fcc and liquid phases barely impact the Pd-Rh phase diagram. The miscibility gap between in the fcc-(Pd,Rh) phase and the solidus and liquidus temperature are still the same. In the Pd-Rh system, both fcc end-members are immiscible at T < 1193 K and the solidus and liquidus temperatures are 1957 and 2011 K, respectively.

The binary system Rh-O was previously studied too. As well, further optimization is implemented in this paper, by further studying the Gibbs energy and enthalpy of formation of Rh_2O_3. This new modeling slightly changes the Rh-O phase diagram. The decompositions of Rh_2O_3 and RhO_2 are calculated at 1417 K and 1031 K, respectively. These temperatures are closer to the experimental values – 1403 K and 1033 K [35; 46] – than in the previous assessment.

After a thorough analysis of the available thermodynamic data, the first assessment of the Pd-O system was performed. Using an accurate review of the literature, this modeling predicts the PdO decomposition at 1140 K at p = 1 bar and the oxygen solubility in fcc-Pd at PdO decomposition around 4.10^{-2} at.% maximum.

The calculated phase diagrams of the ternary system Pd-Rh-O display a very good consistency with the published results. Furthermore, the calculated isotherm at 1000 K considers the stability of RhO_2. This modeling is then a useful calculation tool to predict palladium and rhodium equilibrium phases under any temperature and oxygen pressure conditions.

5. Acknowledgements

The authors acknowledge the funding of the Direction des Programmes Energies of CEA.

The authors thank Nathalie Dupin at Calcul Thermo (http://cthermo.fr/indexen.html) for her valuable comments and fruitful help to develop this Calphad database.

3. CRediT

C. Laurin: Conceptualization, Methodology, Software, Writing-Original draft preparation

A. Quaini: Methodology, Writing-Review & Editing, Project administration

E. Regnier: Conceptualization, Supervision, Validation, Writing-Review & Editing

A. Laplace: Conceptualization, Supervision, Validation, Writing-Review & Editing

T. Croze: Investigation, Writing-Review & Editing

S. Gossé: Supervision, Conceptualization, Methodology, Software, Writing-Original draft preparation

REFERENCES

[1] L. Pattou, J.P. Lorand, M. Gros, Nature 379 (1996) 712-715.

[2] G.B. Haxel, J.B. Hedrick, G.J. Orris, Rare Earth Elements - Critical resources for high technology. in: U.S.G. Survey, (Ed.), 2005.

[3] D.A. Holwell, I. McDonald, Platinum Metals Review 54 (2010) 26-36.

[4] C. Bockrath, C. Ballhaus, A. Holzheid, Science 305 (2004) 1951-1953.

[5] M.E. Fleet, W.E. Stone, J.H. Crocket, Geochimica et Cosmochimica Acta 55 (1991) 2545-2554.

[6] R.W. Powell, R.P. Tye, M.J. Woodman, Platinum metals review 6 (1962) 138-143.

[7] D.J.C. Yates, J.H. Sinfelt, Journal of catalysis 8 (1967) 348-358.

[8] A. Corma, H. Garcia, A. Leyva, Journal of Molecular Catalysis A: Chemical 230 (2005) 97-105.

[9] H. Kleykamp, J.O. Paschoal, R. Pejsa, F. Thommler, Journal of Nuclear Materials 130 (1985) 426-433.

[10] S. Utsunomiya, R.C. Ewing, Radiochimica Acta 94 (2006) 749-753.

[11] Y. Pontillon, G. Ducros, Nuclear Engineering and Design 240 (2010) 1867-1881.

[12] S. Gossé, S. Bordier, C. Guéneau, E. Brackx, R. Domenger, J. Rogez, Journal of Nuclear Materials 500 (2018) 252-264.

[13] J.H. Norman, H.G. Staley, W.E. Bell, Journal of Physical Chemistry 69 (1965) 1373-1376.

[14] C.B. Alcock, G.W. Hooper, Proceedings of the Royal Society of London. Series A 254 (1960) 551-561.

[15] H.D. Schreiber, T.R. Harville, G.N. Damron, Journal of the American Ceramic Society 73 (1990) 1435-1437.

[16] W. Grünewald, G. Roth, W. Tobie, K. Weiß, S. Weisenburger, Glass Technology: European Journal of Glass Science and Technology, Part A 49 (2008) 266-278.

[17] G.E. Rindone, J.L. Rhoads, Journal of the American Ceramic Society 39 (1956) 173-180.

[18] T. Sugawara, T. Ohira, S. Komamine, E. Ochi, Journal of Nuclear Materials 465 (2015) 590-596.

[19] T. Sugawara, T. Ohira, K. Minami, S. Komamine, E. Ochi, Journal of Nuclear Science and Technology 53 (2015) 380-390.

[20] C.J. Capobianco, R.L. Hervig, Solubility of Ru and Pd in silicate melts: the effect of melt composition, Lunar and Planetary Science Conference XXVII, 1996.

[21] A. Holzheid, P. Sylvester, H.S.C. O'Neill, D.C. Ruble, H. Palme, Nature 406 (2000) 396-399.

[22] C. Krause, B. Luckscheiter, J. Mater. Res. 6 (1991) 2535-2546.

[23] T. Hartmann, H. Pentinghaus, Journal of Nuclear Materials 422 (2012) 124-130.

[24] S. Gossé, N. Dupin, C. Guéneau, J.C. Crivello, J.M. Joubert, Journal of Nuclear Materials 474 (2016) 163-173.

[25] H.L. Lukas, S.G. Fries, B. Sundman, Computational Thermodynamics: The Calphad Method, Cambridge University Press, 2007.

[26] M. Hillert, Journal of Alloys and Compounds 320 (2001) 161-176.

[27] B. Sundman, Calphad 15 (1991) 109-119.

[28] O. Redlich, A. Kister, Industrial & Engineering Chemistry 40 (1948).

[29] K.T. Jacob, S. Priya, Journal of Phase Equilibria 19 (1998) 340-350.

[30] K.M. Myles, Transactions of the Metallurgical Society of AIME 242 (1968) 1523-1526.

[31] J.E. Shield, R.K. Williams, Scripta Metallurgica 21 (1987) 1475-1479.

[32] E. Raub, Journal of less common metals 1 (1959) 3-18.

[33] A.A. Rudnitskii, J.M. Yorke, Russian Journal of Inorganic Chemistry 4 (1959) 631-636.

[34] M.H. Kaye, B.J. Lewis, W.T. Thompson, Journal of Nuclear Materials 366 (2007) 8-27.

[35] O. Muller, R. Roy, Journal of the Less Common Metals 16 (1968) 129-146.

[36] J.M.D. Coey, Acta Cryst. B26 (1970) 1876-1877.

[37] J.W.M. Biesterbos, J. Hornstra, Journal of the Less Common Metals 30 (1973) 121-125.

[38] H. Kleykamp, Zeitschrift für Physikalische Chemie 67 (1969) 277-283.

[39] C. Mallika, O.M. Sreedharan, M.S. Chandrasekharaiah, Journal of the Less Common Metals 107 (1985) 203-212.
[40] N.G. Schmahl, E. Minzl, Zeitschrift für Physikalische Chemie Neue Folge 41 (1964) 78-96.
[41] V.K. Tagirov, D.M. Chizhikov, E.K. Kazenas, L.K. Shubochkin, Russian Journal of Inorganic Chemistry 20 (1975) 2035-2037.
[42] J. Nell, H.S.C. O'Neill, Geochimica et Cosmochimica Acta 61 (1997) 4159-4171.
[43] K.T. Jacob, T. Uda, T.H. Okabe, Y. Waseda, High Temperature Materials and Processes 19 (2000) 11-16.
[44] K.T. Jacob, D. Prusty, Journal of Alloys and Compounds 507 (2010) L17-L20.
[45] K.T. Jacob, M.V. Sriram, Metallurgical and Materials Transactions A25 (1994) 1347-1357.
[46] G. Bayer, H.G. Wiedemann, Thermochimica Acta 11 (1975) 79-88.
[47] G. Bayer, H.G. Wiedemann, Thermochimica Acta 15 (1976) 213-226.
[48] K. Reuter, M. Scheffler, Applied Physics A 78 (2004) 793-798.
[49] O. Knacke, O. Kubaschewski, K. Hesselman, Thermodynamical properties of Inorganic substances, Springer, Berlin, Germany, 1991.
[50] I.L. Khodakovskii, N.N. Smirnova, T.A. Bykova, N.A. Polotnyanko, A.V. Kristavchuk, N.D. Shikina, O.V. Karimova, A.V. Mokhov, V.A. Volchenkova, Geochemistry International 49 (2011) 525-530.
[51] N.N. Smirnova, T.A. Bykova, N.A. Polotnyanko, N.D. Shikina, I.L. Khodakovskii, Russian Journal of Physical Chemistry A 84 (2010) 1851-1855.
[52] J. Nell, H.S.C. O'Neill, Geochimica et Cosmochimica Acta 60 (1996) 2487-2493.
[53] K.T. Jacob, T.H. Okabe, T. Uda, Y. Waseda, Journal of Phase Equilibria 20 (1999) 553-564.
[54] O. Kubaschewski, E.L. Evans, C.B. Alcock, Metallurgical thermochemistry, 1967.
[55] Y.K. Rao, Stoichiometry and thermodynamics of metallurgical processes, 1985.
[56] Thermo-Calc, https://www.thermocalc.com/media/4638/db-overview_2013-03-01.pdf - Thermodynamic and mobility databases overview.
[57] C. Mallika, O.M. Sreedharan, J.B. Gnanamoorthy, Journal of less common metals 95 (1983) 213-220.
[58] H. Kleykamp, Zeitschrift für Physikalische Chemie Neue Folge 71 (1970) 142-148.
[59] E. Pawlas-Foryst, L.A. Zabdyr, Archives of Metallurgy and Materials 53 (2008) 1173-1175.
[60] J. Fouletier, G. Vitter, M. Kleitz, Journal of Applied Electrochemistry 5 (1975) 111-120.
[61] V.A. Levitskii, P.B. Narchuk, M.L. Kovba, Y.Y. Skolis, Russian Journal of Physical Chemistry 56 (1982) 1474-1479.
[62] H.J. De Bruin, S.P.S. Badwal, Journal of Solid State Chemistry 34 (1980) 133-135.
[63] W.E. Bell, R.E. Inyard, M. Tagami, The Journal of Physical Chemistry 70 (1966) 3735-3736.
[64] J.S. Warner, Journal of the Electrochemistry Society 114 (1967) 68-71.
[65] K. Persson, Materials Project (2015).
[66] A. Olivei, Journal of the Less-Common Metals 29 (1972) 11-23.
[67] V.I. Rozhdestvina, A.A. Udovenko, S.V. Rubanov, N.V. Mudrovskaya, Crystallography Reports 61 (2016) 193-202.
[68] V.M. Ievlev, S.V. Ryabtsev, A.M. Samoylov, A.V. Shaposhnik, S.B. Kuschev, A.A. Sinelnikov, Sensors and Actuators B: Chemical 255 (2018) 1335-1342.
[69] H. Zhang, J. Gromek, G.W. Fernando, S. Boorse, H.L. Marcus, Journal of Phase Equilibria 23 (2002) 246-248.
[70] J. Gegner, G. Hörz, R. Kirchheim, Journal of Materials Science 44 (2009) 2198-2205.
[71] D. Wang, T.B. Flanagan, Scripta Materialia 49 (2003) 77-80.
[72] J.W. Park, C.J. Altestetter, Scripta Metallurgica 19 (1985) 1481-1485.
[73] E. Raub, W. Plate, Zeitschrift für Metallkunde 48 (1957).
[74] H. Jehn, E. Grallath, Solid solubility of oxygen in palladium - Precious metals: mining, extraction, and processing, AIME Annual Meeting, Los Angeles, 1984.
[75] T. Matsui, K. Naito, Journal of Nuclear Science and Technology 26 (1989) 1102-1111.
[76] R. Gürler, L.A. Cornish, J.N. Pratt, Journal of Alloys and Compounds 191 (1993) 165-168.

Appendix I

Thermodynamic models and list of the optimized parameters

Phase	Sublattice model ***Prototype***	Thermodynamic Parameters / J.mol^{-1}	Reference
Pd, Rh fcc	$(Pd,Rh)_1(O,Va)_1$ ***Cu***	${}^0L^{fcc}_{Pd,Rh:Va} = 24746 - 4.17 \cdot T$ ${}^1L^{fcc}_{Pd,Rh:Va} = -2025 + 0.92 \cdot T$ ${}^0L^{fcc}_{Pd:O} = G^{\circ,PdO} + 50835$ ${}^0L^{fcc}_{Pd:O,Va} = +21600$	Present work
Pd, Rh hcp	$(Pd,Rh)_1(Va)_{0.5}$	${}^0L^{hcp}_{Pd,Rh:Va} = +26701$ ${}^0L^{hcp}_{Pd,Rh:Va} = +7969$	Gossé et al. [24]
Liquid	$(Pd^{+2}, Rh^{+3})_P(O^{-2},Va^{-Q})_Q$	${}^0L^{Liq}_{Pd,Rh} = +13418.5$ $G^{\circ,liquid}_{Pd^{+2}:O^{-2}} - 2 \cdot H^{\circ,SER}_{Pd} - 2 \cdot H^{\circ,SER}_{O} = -120000 + 120 \cdot T - 44.45 \cdot T \cdot \ln(T) - 0.0057 \cdot T^2 + 1.12295 \cdot 10^{-7} \cdot T^3 + 333220 \cdot T^{-1}$ ${}^0L^{liquid}_{Pd^{+2}:O^{-2}} =$+500000 ${}^0L^{liquid}_{Rh^{+3}:O^{-2}} =$+500000	Present work
Rh_2O_3 Orthorombic	$(Rh^{+3})_2(O^{-2})_3$ ***Rh_2O_3***	$G^{\circ,Rh_2O_3}_{Rh^{+3}:O^{-2}} - 2 \cdot H^{\circ,SER}_{Rh} - 3 \cdot H^{\circ,SER}_{O} = -442986 + 708.357 \cdot T - 115 \cdot T \cdot ln(T) - 0.00921 \cdot T^2 + 1399816 \cdot T^{-1}$	Present work
RhO_2 (Rutile)	$(Rh^{+4})_1(O^{-2})_2$ ***TiO_2***	$G^{\circ,Rutile}_{Rh^{+4}:O^{-2}} - H^{\circ,SER}_{Rh} - 2 \cdot H^{\circ,SER}_{O} = -270089 + 464.880 \cdot T + {}^2/_3\, GC_p^{Rh_2O_3} - {}^1/_3\, GH^{SER}_{Rh}$ With: $GC_p^{Rh_2O_3} = -115 \cdot T \cdot \ln(T) - 0.00921 \cdot T^2 + 1399816 \cdot T^{-1}$	Present work
PdO (PtS)	$(Pd^{+2})_1(O^{-2})_1$ ***PtS***	$G^{\circ,PdO}_{Pd^{+2}:O^{-2}} - H^{\circ,SER}_{Pd} - H^{\circ,SER}_{O} = -134604.26 + 273.218 \cdot T - 44.748 \cdot T \cdot \ln(T) - 0.00569 \cdot T^2 + 1.12295 \cdot 10^{-7} \cdot T^3 + 413571 \cdot T^{-1}$	Present work